PASJ: Publ. Astron. Soc. Japan , 1–??,

© 2012. Astronomical Society of Japan.

arXiv:1209.0067v2 [astro-ph.HE] 10 Oct 2012

The K-shell Line Distribution of Heavy Elements along the Galactic Plane Observed with Suzaku

Hideki Uchiyama,[1] Masayoshi Nobukawa,[2,3] Takeshi Go Tsuru,[3] and Katsuji Koyama[3,4]
[1] *Department of Physics, Graduate School of Science, The University of Tokyo, 7-3-1 Hongo, Bunkyo-ku, Tokyo 113-0033*
[2] *The Hakubi Center for Advanced Research, Kyoto University, Yoshida-Ushinomiya-cho, Kyoto 606-8302*
[3] *Department of Physics, Graduate school of Science, Kyoto University, Oiwake-cho, Kitashirakawa, Kyoto 606-8502*
[4] *Department of Earth and Space Science, Graduate School of Science, Osaka University, 1-1 Machikaneyama, Toyonaka, Osaka 560-0043*
uchiyama@juno.phys.s.u-tokyo.ac.jp

(Received ; accepted)

Abstract

We report the global distribution of the intensities of the K-shell lines from the He-like and H-like ions of S, Ar, Ca and Fe along the Galactic plane. From the profiles, we clearly separate the Galactic center X-ray emission (GCXE) and the Galactic ridge X-ray emission (GRXE). The intensity profiles of the He-like Kα lines of S, Ar, Ca and Fe along the Galactic plane are approximately similar with each other, while not for the H-like Lyα lines. In particular, the profiles of H-like Lyα of S and Fe show remarkable contrast; a large excess of Fe and almost no excess of S lines in the GCXE compared to the GRXE. Although the prominent K-shell lines are represented by $\sim$1 keV and $\sim$7 keV temperature plasmas, these two temperatures are not equal between the GCXE and GRXE. In fact, the spectral analysis of the GCXE and GRXE revealed that the $\sim$1 keV plasma in the GCXE has lower temperature than that in the GRXE, and vice versa for the $\sim$7 keV plasma.

Key words: Galaxy: Center—Inter stellar medium— X-ray spectra

1. Introduction

The HEAO-1 satellite discovered unresolved X-ray emissions from the inner disk of the Milky Way (Worrall et al. 1982), which were designated as the Galactic ridge X-ray emission (GRXE). The EXOSAT satellite found that the GRXE was extended by about ±60° in the longitude and ±1°– 2° in the latitude (Warwick et al. 1985). The Tenma satellite discovered a strong emission line at the energy of about 6.7 keV (the 6.7-keV line) in the GRXE (Koyama et al. 1986b). The Ginga satellite made survey observations along the Galactic plane with the 6.7-keV line, and found a prominent peak at the Galactic center extending about 1° (Galactic center X-ray emission, GCXE; Koyama et al. 1989, Yamauchi et al. 1990, Yamauchi & Koyama 1993). Subsequently, the 6.7-keV line was found to consist of three lines at 6.4, 6.7 and 7.0 keV, which are Kα lines of neutral Kα, He-like Kα, and H-like Lyα of irons, respectively (Koyama et al. 1996, Ebisawa et al 2008).

The strong He-like Kα and H-like Lyα lines of iron indicate the presence of hot plasma with a temperature of $kT \sim$5–10 keV. Two possibilities of the origin of the hot plasma have been proposed by many authors. One is true diffuse plasma which fills in the Galactic plane. A problem of this scenario is the energy source. The total energy of the plasma is estimated to be $\sim 10^{56}$ erg. Such a high-temperature plasma cannot be gravitationally bounded in the Galactic plane. The escape time scale is estimated to be a few times 10^5 yr. Thus huge energy input ($\sim$0.1 supernova yr^{-1}) is required to keep the plasma (e.g. Koyama et al. 1986a). The other possibility is that the GCXE and GRXE are superposition of unresolved faint X-ray point sources (Revnivtsev et al. 2009). However, point sources with iron lines, like cataclysmic variables and active binaries, cannot explain large equivalent widths of the iron lines in the GCXE and GRXE (e.g. Yamauchi et al. 2009). Also the spatial distribution of the He-like Kα line of iron shows a larger excess than the stellar mass distribution at the Galactic center region (Uchiyama et al. 2011). True origin would be a mixture of diffuse plasma and point sources, but the mixing ratios are unclear both for the GRXE and GCXE (see Muno et al. 2004, Ebisawa et al. 2005, Koyama et al. 2009, Revnivtsev et al. 2007, Revnivtsev et al. 2009).

Spectral and spatial structures of the GCXE and GRXE plasmas are key information to reveal the origins. Kaneda et al. (1997) found that the GRXE consists of two plasmas of about 0.8 and 7 keV temperatures. Similar two- or multi-temperature structures were revealed for the GCXE (Muno et al. 2004, Ryu et al. 2009, Nobukawa et al. 2010) and the intermediate region between the GCXE and GRXE (Yuasa et al. 2012). The intensity ratio of the He-like and H-like lines from the same atom gives the plasma temperature responsible for these line emissions. Thus the two plasmas structures in the GCXE and GRXE, in the temperature and mixing ratio, would be resolved by the line intensities from many elements and their ratios of the same atom. This paper reports the intensity profiles along the Galactic plane in the He-like Kα and H-like Lyα for

S, Ar, Ca and Fe for the first time. Based on the profiles, we discuss possible origins for the GCXE and GRXE. In this paper, uncertainties are quoted at the 1σ confidence range unless otherwise stated.

2. Observations and Data Reduction

The observations were made with the X-ray Imaging Spectrometer (XIS; Koyama et al. 2007a) on the focal plane of the X-ray telescope (XRT; Serlemitsos et al. 2007) onboard the Suzaku satellite (Mitsuda et al. 2007). The XIS contains four sets of X-ray CCD camera systems (XIS 0, 1, 2, and 3). XIS 0, 2, and 3 have front-illuminated (FI) CCDs, while XIS 1 has a back-illuminated (BI) CCD. The XIS 2 has been out of function since November 2006. Although the CCD chips were significantly degraded by on-orbit particle radiation, the XIS performance had been calibrated well with the checker-flag charge-injection method (Nakajima et al. 2008, Ozawa et al. 2009) until October 2006, and since then, it has been restored with the spaced-row charge-injection method (Prigozhin et al. 2008, Uchiyama et al. 2009). As a result, the energy resolutions were kept within 130–180 eV (FWHM) at 5.9 keV during the observations.

In this paper, we included the data of the series of the Key and Large projects and many ordinary proposals targeted on the Galactic center region. The early reports on the results from these observations are found in the published papers (e.g. Koyama et al. 2007c, Yuasa et al. 2012). As for the GRXE, one can refer to the papers by Ebisawa et al (2008) and Yamauchi et al. (2009). In addition to these data, we collected all the archival Suzaku observations targeted on the Galactic plane of $|b| < 5^\circ$ between August 2005 and March 2011.

We downloaded all the archival data of $|b| < 5^\circ$ from ISAS DARTS[1], then the data reductions were made uniformly on all the data-sets including previously published data-sets. We used the pipeline-processed cleaned data provided by the DARTS site, and made images of the respective data in the 0.5–4 keV and 4–10 keV bands. Based on the X-ray images, we selected the fields with no bright point or diffuse sources. The selected data are listed in table 1. In the following analyses (next section), the raw X-ray spectra including the cosmic X-ray background (CXB) were made from the central area with a circle of $8'.9$ radius by subtracting the NXB with the same COR of the source data. The non X-ray background (NXB) spectra sorted by the cut-off rigidity (COR) were made from the many data sets pointing to the night earth using `xisnxbgen` (Tawa et al. 2008)

Using `xissimarfgen` (Ishisaki et al. 2007) and `xisrmfgen`, the effective area of the XRT and the response of the XIS were calculated, and ancillary response files and redistribution matrix files were made for respective observations. Since the responses of the FIs are almost the same, we merged the FI spectra. The BI data were not used because the NXB flux is high above the Fe line bands.

3. Analyses

3.1. The Line Intensities

We made the NXB-subtracted X-ray spectra of the GCXE and GRXE, and found many prominent lines as is shown in figure 7 for example. From the center energies, we identified these lines as the K-shell lines from He- and H-like Ne, Mg, Si, S, Ar, Ca and Fe ions. We also identified a prominent K-shell line from neutral Fe (Fe I Kα). According to Ryu et al. (2009), especially in the Galactic center region, the foreground emission dominates below the 2 keV band. In order to avoid the contamination of the foreground emission and to extract the line intensities from the GCXE and GRXE, we separately fitted the spectra in the 2.3–5 and 5–8 keV bands with a phenomenological model, an absorbed power-law continuum plus nine (for the 2.3–5 keV band) or four (for the 5–8 keV band) narrow Gaussians.

The line center energies of the Gaussians were fixed to be 2.45 (S XV Kα), 2.62 (S XVI Lyα), 2.88 (S XV Kβ), 3.12 (Ar XVII Kα), 3.32 (Ar XVIII Lyα), 3.70 (Ar XVII Kβ), 3.89 (Ca XIX Kα), 4.11 (Ca XX Lyα) and 4.59 (Ca XIX Kβ) for the 2.3–5 keV band, and 6.40 (Fe I Kα), 6.68 (Fe XX Kα), 6.97 (Fe XXI Lyα) and 7.06 keV (Fe I Kβ) for the 5–8 keV band, according to Smith et al. (2001; APEC model) and Kaastra & Mewe (1993). The intensities of the lines were left free except for Fe I Kβ, which was fixed to 0.125 times that of the Fe I Kα line according to Kaastra & Mewe (1993). The normalization, photon index, and interstellar absorption in the absorbed power-law component were also left free. The cross section of the photoelectric absorption was obtained from Morrison & McCammon (1983). Using the phenomenological model, we obtained the intensities of the He-like Kα and H-like Lyα lines of S, Ar, Ca, and Fe. We also extracted the intensities in the 2.3–5 keV and 5–8 keV bands, and that of Fe I Kα line. An example of the spectra and the best-fit models is shown in figure 1.

3.2. Intensity profiles of the continuums and lines

Using the best-fit intensities, we constructed the line intensity distributions along the Galactic plane as a function of angular distance from the Galactic center (Sgr A*). In the following description, we adopted a new coordinate as $(l_*, b_*) = (l + 0^\circ.056,\ b + 0^\circ.046)$, where the origin of this coordinate $(l_*, b_*) = (0^\circ, 0^\circ)$ is the position of Sgr A* (Reid & Brunthaler 2004) and the $b_* = 0^\circ$ line corresponds to the Galactic plane.

The line intensity profiles were fitted with a phenomenological model given by

$$I(l_*, b_*) = I_\mathrm{C} \times \exp\left(-\frac{|l_*|}{l_\mathrm{C}}\right) \times \exp\left(-\frac{|b_*|}{b_\mathrm{C}}\right) + I_\mathrm{R} \times \exp\left(-\frac{|l_*|}{l_\mathrm{R}}\right) \times \exp\left(-\frac{|b_*|}{b_\mathrm{R}}\right), \qquad (1)$$

where the first and the second terms of the right side of

---

[1] http://darts.jaxa.jp/

Table 1. Observation data list.

OBSID	Pointing direction				Observation		Exp.	Object name	Spectra*
	$\alpha_{2000.0}(^\circ)$	$\delta_{2000.0}(^\circ)$	$l(^\circ)$	$b(^\circ)$	Start (UT)	End (UT)	(ks)		
100028020	243.66	-51.18	-28.00	-0.15	2005-09-18T22:47:36	2005-09-19T11:58:41	19.3	HESS J1616-508 BGD1	GRXE
100028030	244.46	-50.69	-27.30	-0.15	2005-09-20T19:40:17	2005-09-21T07:29:24	21.9	HESS J1616-508 BGD2	
100027020	266.30	-29.17	-0.25	-0.05	2005-09-24T14:17:17	2005-09-25T17:27:19	42.8	Sgr A west	GCXE
100026020	257.38	-38.82	-12.37	0.71	2005-09-25T19:11:40	2005-09-26T15:42:09	34.9	RXJ1713-3946-BKGD1	GRXE
100026030	257.27	-41.04	-14.20	-0.54	2005-09-28T07:09:13	2005-09-29T04:25:24	37.5	RXJ1713-3946-BKGD2	GRXE
100037010	266.30	-29.17	-0.25	-0.05	2005-09-29T04:35:41	2005-09-30T04:29:19	43.7	Sgr A west	GCXE
500009010	281.00	-4.07	28.46	-0.20	2005-10-28T02:40:08	2005-10-30T21:30:15	93.3	GALACTIC RIDGE	
500019010	265.79	-29.89	-1.09	-0.04	2006-02-23T10:51:11	2006-02-23T20:02:19	13.3	SGR C BGD	
500008010	270.96	-22.02	8.04	-0.05	2006-04-07T11:49:16	2006-04-08T10:54:18	40.7	HESS J1804-216 BGD	
500025010	9.24	64.24	121.36	1.41	2006-06-29T15:42:01	2006-06-30T18:15:24	51.0	TYCHO SNR HXD BKGD	
501043010	242.01	-52.44	-29.60	-0.38	2006-09-16T11:02:03	2006-09-17T07:14:14	43.6	HESS J1614-518 BG	GRXE
501009010	266.19	-28.91	-0.07	0.18	2006-09-29T21:26:07	2006-10-01T06:55:19	51.2	GC SOUTH BGD	GCXE
501049010	265.38	-29.75	-1.17	0.33	2006-10-08T10:22:40	2006-10-09T02:19:24	19.6	GALACTIC CENTER	
501051010	265.70	-29.93	-1.17	-0.00	2006-10-09T13:40:09	2006-10-10T06:44:24	21.9	GALACTIC CENTER	
501052010	265.50	-30.21	-1.50	0.00	2006-10-10T06:45:09	2006-10-10T21:18:14	19.3	GALACTIC CENTER	
501053010	265.30	-30.50	-1.83	-0.00	2006-10-10T21:18:59	2006-10-11T10:06:14	21.9	GALACTIC CENTER	
501057010	266.03	-30.11	-1.17	-0.33	2006-10-11T10:07:27	2006-10-12T03:28:14	20.5	GALACTIC CENTER	
500009020	281.00	-4.07	28.46	-0.20	2006-10-15T02:15:12	2006-10-17T19:32:19	98.9	GALACTIC RIDGE	
501046010	265.98	-28.90	-0.17	0.33	2007-03-10T15:03:10	2007-03-11T03:55:14	25.2	GALACTIC CENTER	GCXE
501047010	265.78	-29.19	-0.50	0.33	2007-03-11T03:55:59	2007-03-11T19:04:14	25.6	GALACTIC CENTER GC2	GCXE
501048010	265.58	-29.47	-0.83	0.33	2007-03-11T19:04:59	2007-03-12T08:09:14	27.5	GALACTIC CENTER GC3	GCXE
502021010	113.33	-19.53	-125.00	0.00	2007-04-22T20:39:20	2007-04-25T10:04:24	89.5	ANTICENTER	
502022010	266.81	-28.88	0.23	-0.27	2007-08-31T12:33:33	2007-09-03T19:00:25	134.8	(L,B)=(0.25,-0.27)	GCXE
502053010	275.64	-15.58	15.82	-0.84	2007-10-07T02:16:29	2007-10-08T18:10:14	71.5	M17 EAST BKG	GRXE
502002010	267.16	-29.14	0.17	-0.67	2007-10-09T16:40:54	2007-10-10T03:40:24	23.2	GC14	GCXE
502003010	266.96	-29.42	-0.17	-0.67	2007-10-10T03:41:13	2007-10-10T15:20:24	21.5	GC15	GCXE
502004010	267.48	-29.31	0.17	-1.00	2007-10-10T15:21:17	2007-10-11T01:00:24	19.9	GC16	GCXE
502005010	267.29	-29.60	-0.17	-1.00	2007-10-11T01:01:17	2007-10-11T11:32:20	20.6	GC17	GCXE
502006010	266.18	-28.62	0.17	0.33	2007-10-11T11:34:01	2007-10-11T23:07:14	22.6	GC18	GCXE
502007010	265.86	-28.45	0.17	0.67	2007-10-11T23:09:15	2007-10-12T09:52:14	22.0	GC19	GCXE
502011010	266.57	-28.05	0.83	0.33	2007-10-13T18:51:09	2007-10-14T05:30:24	23.0	GC23	GCXE
503006010	13.00	62.90	123.00	0.03	2008-08-01T00:17:23	2008-08-02T20:11:19	86.1	ANTICENTER2	
503007010	266.44	-28.57	0.33	0.17	2008-09-02T10:15:27	2008-09-03T22:52:24	52.2	GC LARGEPROJECT1	GCXE
503008010	266.78	-29.13	0.00	-0.38	2008-09-03T22:53:29	2008-09-05T06:56:19	53.7	GC LARGEPROJECT2	GCXE
503010010	266.04	-29.55	-0.70	-0.05	2008-09-06T15:56:13	2008-09-08T01:39:24	53.1	GC LARGEPROJECT4	GCXE
503013010	265.67	-30.07	-1.30	-0.05	2008-09-16T00:51:19	2008-09-18T04:44:24	104.8	GC LARGEPROJECT7	
503014010	265.18	-30.75	-2.10	-0.05	2008-09-18T04:46:49	2008-09-19T07:32:20	55.4	GC LARGEPROJECT8	GRXE
503015010	265.03	-30.96	-2.35	-0.05	2008-09-19T07:33:05	2008-09-20T09:56:13	56.8	GC LARGEPROJECT9	GRXE
503016010	264.87	-31.17	-2.60	-0.05	2008-09-22T06:47:49	2008-09-23T08:07:17	52.2	GC LARGEPROJECT10	GRXE
503017010	264.72	-31.38	-2.85	-0.05	2008-09-23T08:08:10	2008-09-24T09:21:13	51.3	GC LARGEPROJECT11	GRXE
503018010	264.56	-31.60	-3.10	-0.05	2008-09-24T09:27:54	2008-09-24T22:30:24	29.4	GC LARGEPROJECT12	
503018020	264.56	-31.60	-3.10	-0.05	2008-10-03T18:05:13	2008-10-04T03:42:18	12.2	GC LARGEPROJECT12	
503018030	264.56	-31.60	-3.10	-0.05	2009-02-19T07:32:01	2009-02-19T16:36:24	11.9	GC LARGEPROJECT12	GRXE
503019010	264.40	-31.81	-3.35	-0.05	2009-02-19T16:37:49	2009-02-21T01:15:14	52.8	GC LARGEPROJECT13	
503020010	264.24	-32.02	-3.60	-0.05	2009-02-21T01:15:55	2009-02-22T18:59:14	61.1	GC LARGEPROJECT14	
503072010	265.99	-29.21	-0.42	0.17	2009-03-06T02:39:12	2009-03-09T02:55:25	140.6	EXTENDED CHIMNEY	GCXE
503099010	265.18	-28.53	-0.22	1.13	2009-03-10T19:39:08	2009-03-11T10:56:14	29.7	GCL1	GCXE
503101010	265.27	-28.86	-0.45	0.88	2009-03-16T14:43:17	2009-03-17T07:48:24	33.9	GCL3	GCXE
503102010	265.35	-29.19	-0.70	0.65	2009-03-17T07:49:09	2009-03-18T01:42:24	33.7	GCL4	GCXE
503022010	263.25	-31.95	-4.00	0.70	2009-03-18T23:11:24	2009-03-19T21:26:24	41.3	LOOP 1 L=356.00	GRXE
503023010	263.46	-31.67	-3.67	0.70	2009-03-26T06:37:01	2009-03-27T01:53:19	31.2	LOOP 2 L=356.33	
504093010	268.30	-31.66	-1.50	-2.80	2009-09-17T13:54:31	2009-09-19T03:37:14	53.2	GALACTIC BULGE10	
504089010	267.55	-29.60	-0.05	-1.20	2009-10-09T04:05:59	2009-10-10T14:10:06	55.3	GALACTIC BULGE2	
504090010	266.69	-30.84	-1.50	-1.20	2009-10-13T04:17:20	2009-10-14T11:29:06	41.3	GALACTIC BULGE7	
504088010	267.22	-29.37	-0.00	-0.83	2009-10-14T11:30:56	2009-10-15T15:29:19	47.2	GALACTIC BULGE1	GCXE
505080010	270.15	-30.91	-0.05	-3.80	2010-04-07T17:15:10	2010-04-09T21:14:16	56.1	GALACTIC BULGE5	
505083010	264.99	-32.42	-3.60	-0.80	2010-10-10T14:04:38	2010-10-11T21:33:13	52.9	GALACTIC BULGE14	
505078010	267.95	-29.80	-0.05	-1.60	2011-03-04T19:13:55	2011-03-06T05:30:11	51.3	GALACTIC BULGE3	
505084010	265.70	-32.79	-3.60	-1.50	2011-03-06T05:36:44	2011-03-07T13:01:11	50.3	GALACTIC BULGE15	
505079010	269.15	-30.41	-0.05	-2.80	2011-03-12T06:36:20	2011-03-13T10:17:21	50.2	GALACTIC BULGE4	
505087010	269.31	-34.58	-3.60	-5.00	2011-03-13T10:20:22	2011-03-14T12:39:21	51.5	GALACTIC BULGE18	
505082010	264.59	-32.21	-3.60	-0.40	2011-03-15T13:54:28	2011-03-16T14:54:23	48.5	GALACTIC BULGE13	GRXE

* This column shows whether the data were used to make the mean GCXE or GRXE spectra in figure 8 (see section 3.3).

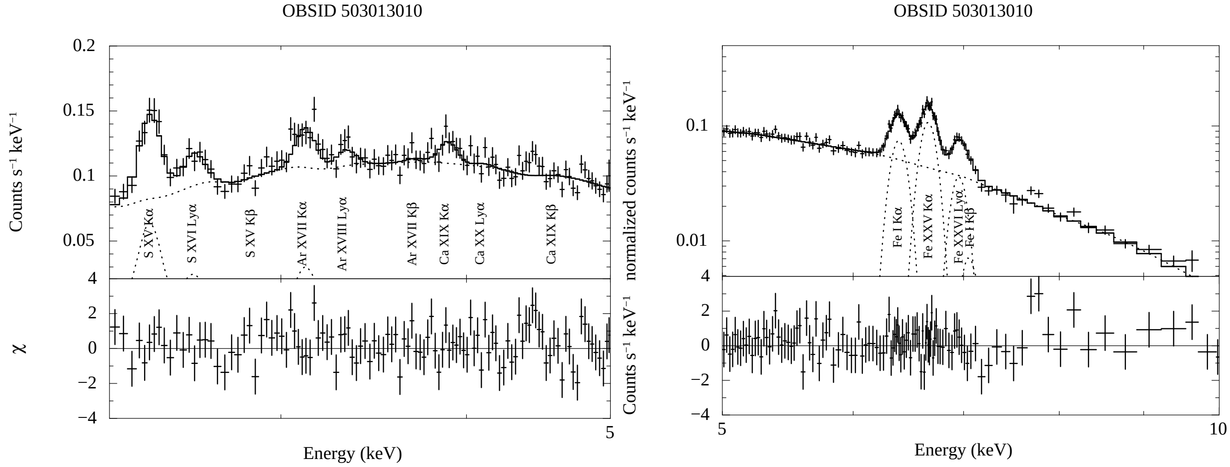

Fig. 1. Left : An example of the spectra with the best-fit phenomenological model in the 2.3–5 keV band (OBSID 503013010). We also show the positions of the lines included in the model. Right : the same as the left panel, but that in the 5–10 keV.

equation 1 represent the intensity profiles of the GCXE and GRXE, respectively. The parameters $l_{\rm C}$ and $l_{\rm R}$ are the e-folding scale lengths along the Galactic plane, while the parameters $b_{\rm C}$ and $b_{\rm R}$ are the e-folding scale heights perpendicular to the Galactic plane, for the GCXE and GRXE, respectively.

At first, we fitted the line intensity profiles with free parameters of $I_{\rm C}$, $I_{\rm R}$, $l_{\rm C}$, $l_{\rm R}$, $b_{\rm C}$ and $b_{\rm R}$ for all the elements independently. Then the parameters for S XV Kα and Fe XXV Kα were well constrained with relatively small errors, while those of the other lines had large errors. In detail, the scale heights $b_{\rm C}$ and $b_{\rm R}$ for S XVI Lyα, Ar XVII Kα and Ca XIX Kα were $\sim 0\overset{\circ}{.}4$ and 4°, near to the same values of S XV Kα. Those for Ar XVIII Lyα, Ca XX Lyα, and Fe XXVI Lyα were $\sim 0\overset{\circ}{.}3$ and 3°, near to the same values of Fe XXV Kα. We therefore linked these parameters with two groups; "S XV Kα" and "Fe XXV Kα" groups, as shown in table 2. The spectral analyses in the next section support that the two groups roughly correspond to the low temperature plasma (LP) and high temperature plasma (HP), respectively (see figure 7). Finally, we re-fitted the line intensity profiles simultaneously with the constraints mentioned above. Then all the profiles were still nicely described with the two-exponential model (equation 1) within reasonable errors of the relevant parameters. The best-fit parameters are summarized in table 2.

For the S and Fe lines, the intensity normalizations of the GCXE and GRXE ($I_{\rm C}$ and $I_{\rm R}$) were well determined. The ratios of Fe XXVI Lyα to Fe XXV Kα (Lyα/Kα) are 0.45 ± 0.06 and 0.20 ± 0.08 in the GCXE and GRXE, respectively, which indicate the plasma temperatures are respectively ~ 8 and ~ 5 keV, respectively. On the other hand, those of S XVI Lyα to S XV Kα are < 0.09 and 0.37 ± 0.14 in the GCXE and GRXE, respectively. Therefore the respective plasma temperatures are $kT < 1$ keV and $kT \sim$ 1.3–1.6 keV. These facts support that the GCXE and GRXE consist of, at least, two-temperature plasmas as already reported by the previous works (see introduction).

The Fe I Kα line should be emitted by cold neutral matter and have a different origin from the above thermal lines. Therefore we fitted its intensity profile separately. We also fitted the intensity profiles of the 2.3–5 and 5–8 keV bands with the same phenomenological model but including the contribution of the CXB. The spectrum and intensity of the CXB were estimated according to Kushino et al. (2002) with an absorption of $N_{\rm H} = 6 \times 10^{22}$ cm^{-2} (Ebisawa et al. 2001, Yamauchi et al. 2009). These best-fit parameters are also listed in table 2.

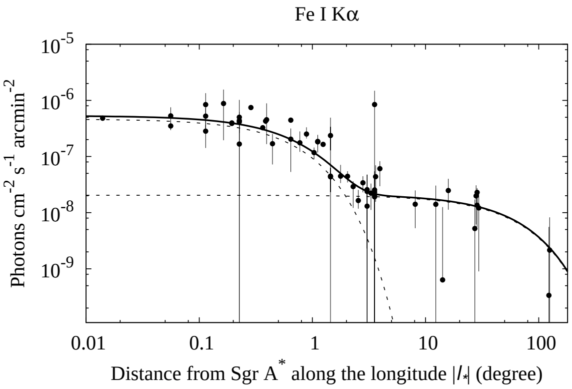

Fig. 3. Intensity distribution of the Fe I Kα line along the Galactic plane.

The intensity distributions of S, Ar, Ca and Fe along the Galactic plane were shown in figures 2 and 3. Also the 2.3–5 keV and 5–8 keV band intensities are given in figure 4 together with the best-fit models. In these figures, all the data points were multiplied by factors of $I(l_*, 0)/I(l_*, b_*)$ to correct the intensity dependence along the latitude.

From figures 1, 2 and table 1, we demonstrate a clear separation of the GCXE and GRXE. The GCXE is concentrated near the Galactic center (Sgr A*) with e-folding parameters of about $0\overset{\circ}{.}6$ ($l_{\rm C}$ in table 2) along the longitude. The latitude extension ($b_{\rm C}$; scale height) is about $0\overset{\circ}{.}2$–$0\overset{\circ}{.}4$. The GRXE is more extended with the e-folding

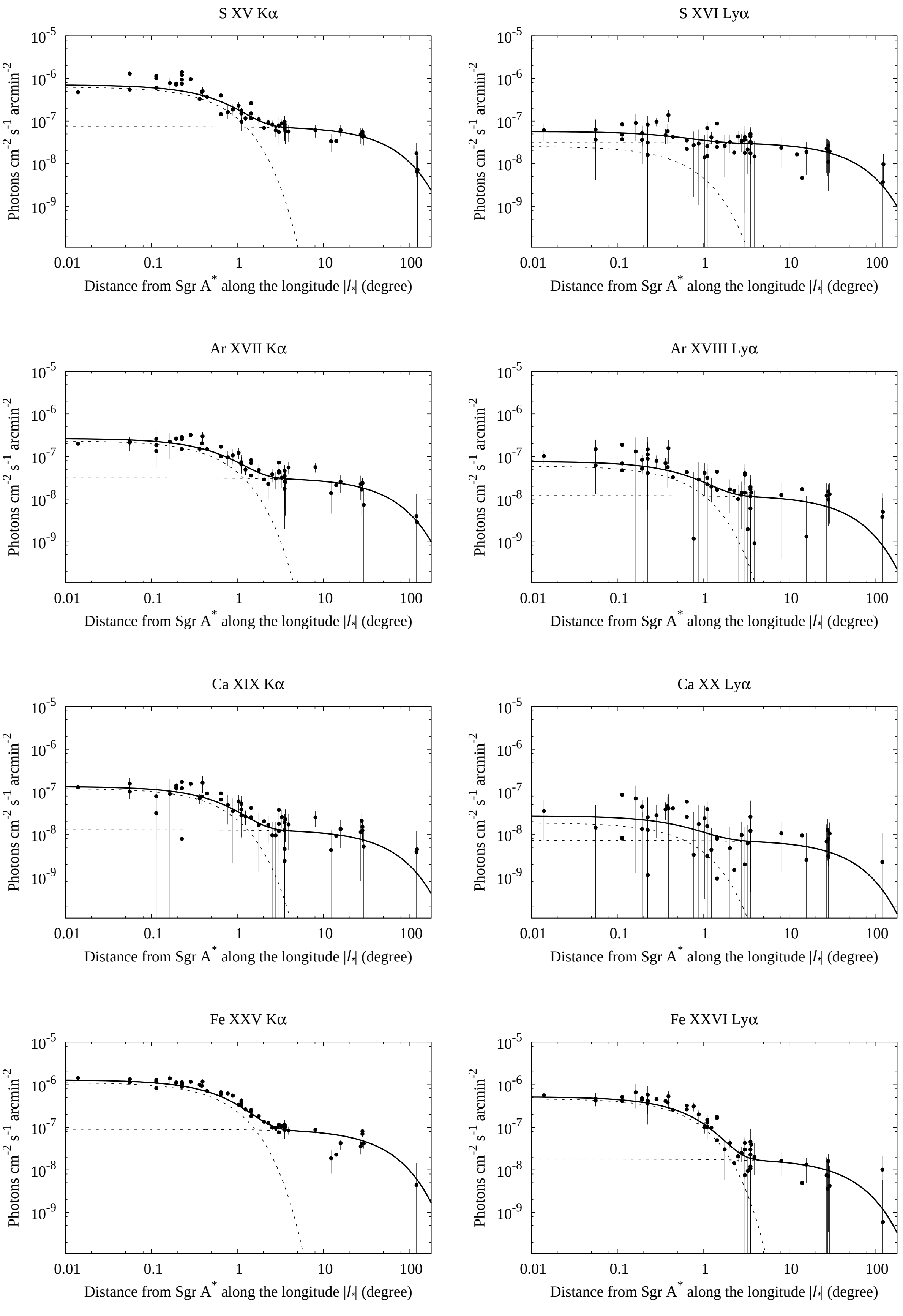
S XV Kα

S XVI Lyα

Ar XVII Kα

Ar XVIII Lyα

Ca XIX Kα

Ca XX Lyα

Fe XXV Kα

Fe XXVI Lyα

Fig. 2. Intensity distributions of the K-shell lines of Fe, Ca, Ar and S along the Galactic plane.

Table 2. Best-fit parameters of the two-exponential model.

	$I_{\rm C}$*	I_R*	$I_{\rm C}/I_{\rm R}$	$l_{\rm C}$ (degree)	$b_{\rm C}$ (degree)	$l_{\rm R}$ (degree)	$b_{\rm R}$ (degree)
S XV Kα	7.78 ± 0.47	0.75 ± 0.08	10 ± 1	0.58 ± 0.05	0.43 ± 0.03	52 ± 13	4.1 ± 1.3
S XVI Lyα	0.31 ± 0.24	0.32 ± 0.05	1.0 ± 0.8	0.58†	0.43†	52†	4.1†
Ar XVII Kα	2.86 ± 0.24	0.32 ± 0.05	9 ± 2	0.58†	0.43†	52†	4.1†
Ar XVIII Lyα	0.78 ± 0.21	0.12 ± 0.03	7 ± 2	0.63‡	0.27‡	45‡	2.9‡
Ca XIX Kα	1.48 ± 0.19	0.13 ± 0.03	11 ± 3	0.58†	0.43†	52†	4.1†
Ca XX Lyα	0.24 ± 0.18	0.07 ± 0.03	3.4 ± 3.0	0.63‡	0.27‡	45‡	2.9‡
Fe XXV Kα	14.57 ± 0.47	0.91 ± 0.08	16 ± 2	0.63 ± 0.03	0.27 ± 0.01	45 ± 10	2.9 ± 0.5
Fe XXVI Lyα	6.08 ± 0.30	0.18 ± 0.04	34 ± 7	0.63‡	0.27‡	45‡	2.9‡
Fe I Kα	6.2 ± 0.6	0.21 ± 0.09	29 ± 13	0.62 ± 0.09	0.23 ± 0.03	57 ± 50	1.1 ± 0.6
2.3–5 keV	126 ± 15	16 ± 1	8 ± 1	0.63 ± 0.07	0.42 ± 0.04	59 ± 6	4.9 ± 0.8
5–8 keV	101 ± 11	6.2 ± 0.6	16 ± 2	0.72 ± 0.06	0.31 ± 0.02	52 ± 9	2.8 ± 0.5

* The units are 10^{-7} photons s^{-1} cm^{-2} arcmin^{-2}. The interstellar absorption is not corrected.

† These e-folding scale lengths and scale heights are linked to those of S XV Kα.

‡ These e-folding scale lengths and scale heights are linked to those of Fe XXV Kα.

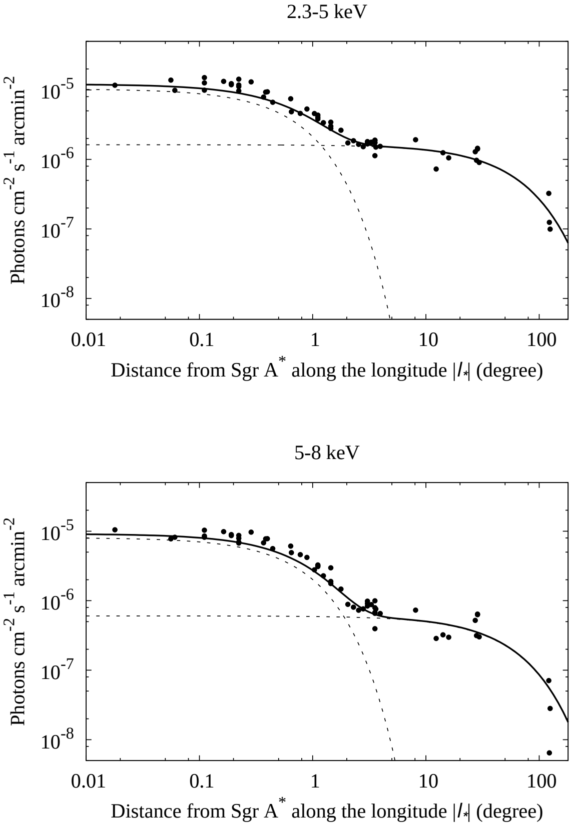

Fig. 4. Intensity distributions of the X-ray flues in the 2.3–5 keV (top) and 5–8 keV bands (bottom) along the Galactic plane.

parameters of ~50° in the longitude and the scale heights of about 1°–5° in the latitude .

The intensities at the center from the GCXE and GRXE are given with the parameters $I_{\rm C}$ and $I_{\rm R}$, respectively. In order to see systematic trends of the $I_{\rm C}/I_{\rm R}$ ratios, we plotted the ratio in figure 5 as a function of atomic number. For the He-like Kα lines, all the elements have roughly equal values of $I_{\rm C}/I_{\rm R} \sim 10$–20, while the H-like Ly$\alpha$ lines are largely scattered among the elements. These phenomena are not due to the difference of interstellar absorption ($N_{\rm H}$) between the GCXE and GRXE, because the He-like Kα and H-like Lyα lines show different trends. The observed S line intensities may be reduced by the large $N_{\rm H}$. The averaged $N_{\rm H}$ of the GCXE and GRXE are 6×10^{22} and 4×10^{22} cm^{-2}, respectively (see section 3.3). Then the Kα lines are absorbed by 80% and 66%, while S XVI Lyα lines are 70% and 55%, for the GCXE and GRXE, respectively. Thus the correction factors on the ratio of $I_{\rm C}/I_{\rm R}$ due to the $N_{\rm H}$ absorption are 1.7 and 1.5 for the GCXE and GRXE, respectively, and hence give no significant change on the trends in figure 4.

A remarkable contrast is found in the profiles of the Fe XXVI Lyα and S XVI Lyα lines. The $I_{\rm C}/I_{\rm R}$ of S XVI Lyα is ~1 and hence there is no clear excess of S XVI Lyα in the GCXE, while that of Fe XXVI Lyα is ~34 times larger than that in the GRXE. These structures may be attributable to a complex plasma structure in the GCXE and GRXE (see discussion).

The complex plasma structure is also noted in the intensity ratios of H-like Lyα/He-like Kα for the elements in the GCXE and GRXE (figure 6). This figure indicates that the ionization states of S, Ar and Ca are higher in the plasma of the GRXE than those in the GCXE, while visa versa for the ionization state of Fe. In the next section, we present a quantitative analysis for the complexity of the GCXE and GRXE plasmas.

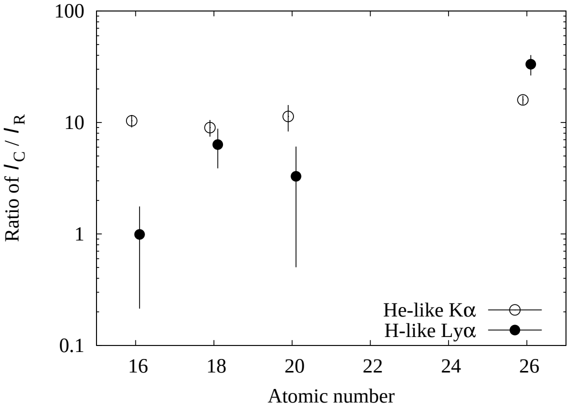

Fig. 5. Intensity ratio of the GCXE to GRXE ($I_{\rm C}/I_{\rm R}$) as a function of atomic numbers.

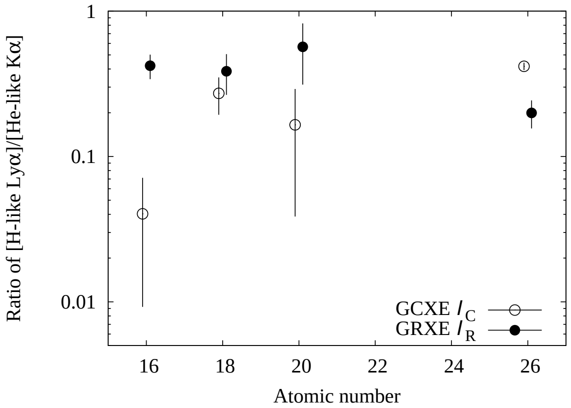

Fig. 6. Intensity ratio of H-like Lyα/He-like Kα for the GCXE and GRXE as a function of atomic numbers.

3.3. Two-temperature structures for the GCXE and GRXE

Since we were able to divide the GCXE and GRXE regions in the line-intensity distributions, mean X-ray spectra of the GCXE and GRXE were separately made using the data sets from the regions of ($|l| < 1^{\circ}$, $|b| < 0.^{\circ}5$) and ($|l| > 2^{\circ}$, $|b| < 0.^{\circ}5$), respectively.

Although we selected data regions with no-bright source by eyes (section 2), some faint sources might contaminate the selected data. To exclude this possibly contaminated data, we calculated standard deviations of $(I_{\rm data} - I_{\rm model})/I_{\rm model}$, where $I_{\rm data}$ and $I_{\rm model}$ are the continuum intensities of the data and the predicted values by the best-fit two-exponential model, in the 2.3–5 keV and 5–8 keV bands (figure 4). The standard deviations (1σ) are 0.34 (2.3–5 keV) and 0.24 (5–8 keV). We excluded the data whose intensities were over the 2σ range in the either 2.3–5 keV or 5–8 keV band. The data used to make the mean spectra are indicated in the last column of table 1. The wide-band spectra of the GCXE and GRXE in the 0.5–10 keV band are given in figure 7 with the black and red marks, respectively. The total exposures of the spectra are 948 (GCXE) and 526 (GRXE) ks.

We see that both of the spectra have a common component below ∼1.2 keV. We fitted the 0.5–1.2 keV band spectra with two-temperature plasmas. The best-fit temperatures are 0.09 ± 0.01 and 0.59 ± 0.01 keV. In this paragraph, errors are estimated at the 90% confidence ranges. The abundance and absorption column density are $Z = 0.05 \pm 0.01$ solar and $N_{\rm H} = 5.6(\pm 0.5) \times 10^{21}$ cm^{-2}, respectively. The 0.5–1.2 keV intensities are 1.1×10^{-6} and 9.7×10^{-7} ph. cm^{-2} s^{-1} arcmin^{-2} for the 0.09 and 0.59 keV components, respectively.

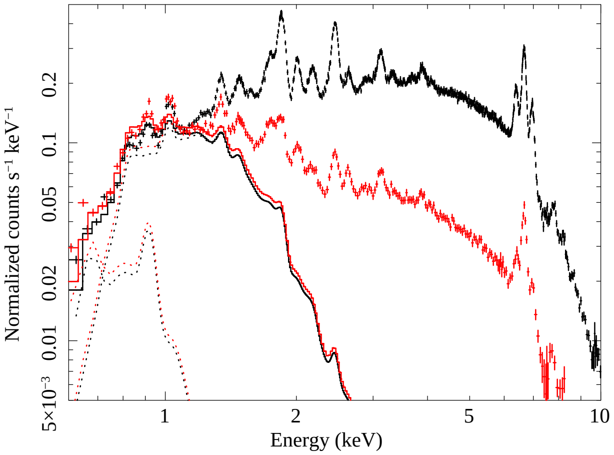

Fig. 7. Wide-band spectra (0.5–10 keV) of GCXE and GRXE (black and red marks, respectively) after the subtraction of the NXB. The model fitted in the 0.5–1.2 keV band is shown in the solid line.

As we found from the fitting with the phenomenological model (section 3.1), the intensity ratios of the He-like Kα and H-like Lyα are different from element to element. The ratios are also different from the GCXE to the GRXE. These facts indicate that the K-shell lines from various atoms cannot be explained by one-temperature plasma but multi-temperature components are required. To investigate the origins of the GCXE and GRXE, we fitted the spectra with a physical model in the relevant energy range of 2.3–10 keV. These fits include the foreground emission with fixed intensity and shape given in figure 7.

Including the Fe I Kα (6.4 keV) line, the plasma needs at least three-temperature components, which are representative for the emission lines of the 6.4 keV (Fe I Kα, cold matter), the 2.45 keV (S XV Kα, low temperature plasma: LP), and the 6.7 keV (Fe XXV Kα, high temperature plasma: HP). Also the spectra include the cosmic X-ray background (CXB). Thus minimum requirements are that the spectra compose of the following four components;

1. High temperature plasma (HP) responsible for the 6.7-keV line.
2. Low temperature plasma (LP) responsible for the 2.45-keV line.
3. Cold matter (CM) component that emits the 6.4-keV line.

4. The cosmic X-ray background (CXB).

We combined the HP and LP and defined as the thermal plasma (TP) given by;

$$\mathrm{TP} = \mathrm{APEC1} + \mathrm{APEC2}\ [\mathrm{ph.\ cm^{-2}\ s^{-1}\ arcmin^{-2}}], \quad (2)$$

where APEC is an optically thin-thermal plasma model by Smith et al. (2001), and APEC1 and APEC2 represent the HP and LP, respectively.

The component 3 possibly originates from bombardment of X-rays, electrons, or protons on cold interstellar gas. We designated as the cold matter component (CM) as;

$$\begin{aligned}\mathrm{CM} = {} & \mathrm{Gaussian1} + \mathrm{Gaussian2} \\ & + A \times (E/\mathrm{keV})^{-\Gamma}\ [\mathrm{ph.\ cm^{-2}\ s^{-1}\ arcmin^{-2}}], \quad (3)\end{aligned}$$

where narrow Gaussians, Gaussian1 and Gaussian2, represent Fe I Kα and Kβ lines, respectively. The line center energy and intensity of Gaussian2 were linked to 1.103 and 0.125 times of those of Gaussian1 (Kaastra & Mewe 1993).

The cosmic X-ray background is compiled by Kushino et al. (2002) as;

$$\begin{aligned}\mathrm{CXB} = {} & 8.2 \times 10^{-7} \\ & \times (E/\mathrm{keV})^{-1.4}\ [\mathrm{ph.\ cm^{-2}\ s^{-1}\ arcmin^{-2}}]. \quad (4)\end{aligned}$$

These components are the subject of absorption, and hence our model to fit the data is;

$$\begin{aligned}\mathrm{MODEL} = {} & \mathrm{Abs1} \times (\mathrm{TP} + \mathrm{Abs2} \times \mathrm{CM} \\ & + \mathrm{Abs1} \times \mathrm{CXB})\ [\mathrm{ph.\ cm^{-2}\ s^{-1}\ arcmin^{-2}}], (5)\end{aligned}$$

where Abs1 is interstellar absorption toward the GCXE or GRXE, and Abs2 is intra-cloud absorption which emits neutral iron lines. The Abs1 multiplies twice on the CXB component because the CXB suffers from interstellar absorption (Abs1) two times: those by the front and back sides of the TP component.

Nobukawa et al. (2010) successfully decomposed the GCXE plasma into the similar components of equation 5. Therefore, we applied this model (equation 5) for the GCXE and GRXE separately. The temperatures of APEC1 and APEC2 were left free, but the abundances are collectively linked, keeping the ratio proportional to the solar abundance (Anders & Grevesse 1989). However the Ar, Ca and Ni lines in the GCXE and the Ar line in the GRXE show excess over the models, we hence made the abundances of these elements free.

For the fitting of the GRXE spectrum in the component 3, photon index and equivalent width (EW) of Fe I Kα ($EW_{6.4}$) were fixed to the best-fit values of the GCXE. The absorption (Abs2) was fixed to be 0 because there is no particularly dense molecular cloud in the GRXE region and thus we assumed that intra-cloud absorption is ignorable. The fitting results for the GCXE and GRXE are shown in figure 8, and the best-fit parameters are listed in table 3.

Table 3. The best-fit physical parameters for the GCXE and GRXE*.

	GCXE	GRXE
N_{H1} (10^{22} cm^{-2})	5.59 ± 0.20	$4.22^{+0.34}_{-0.16}$
N_{H2} (10^{22} cm^{-2})	21 ± 2	0 (fixed)
kT_1 (keV)	$7.38^{+0.05}_{-0.10}$	$6.64^{+0.40}_{-0.42}$
kT_2 (keV)	0.95 ± 0.02	$1.33^{+0.11}_{-0.08}$
Z (solar)	$1.25^{+0.04}_{-0.05}$	$0.81^{+0.15}_{-0.09}$
Z_{Ar} (solar)	$1.73^{+0.11}_{-0.15}$	$1.07^{+0.21}_{-0.20}$
Z_{Ca} (solar)	1.89 ± 0.18	0.81 (linked to Z)
Z_{Ni} (solar)	$2.38^{+0.30}_{-0.32}$	0.81 (linked to Z)
Γ	$2.13^{+0.09}_{-0.10}$	2.13 (fixed)
$EW_{6.4}$ (eV)	457 ± 29	457 (fixed)
$EM1/EM2$†	0.24 ± 0.02	0.29 ± 0.07
χ^2/d.o.f.	755/528=1.43	127/143=0.89

* The uncertainties show the 90% errors.

† Emission measure of the plasma, which is proportional to $n_{\mathrm{e}} n_{\mathrm{H}} V$, where n_{e} and n_{H} are electron and hydrogen densities, respectively, while V is the volume of plasma.

4. Discussion

The intensity ratios of the He-like Kα and the H-like Lyα are different from element to element, and the intensity ratios of these lines in the GCXE are different from the GRXE. The thermal components responsible for these lines are decomposed into, at least two components, the low temperature plasma (LP) and high temperature plasma (HP). The LP temperature in the GRXE is higher than that in the GCXE, while vice versa for the HP. These complex structures indicate that the origins of the GCXE and GRXE would be a mixture of at least two sources with different temperatures. We separately discuss the origins of the HP and LP although these may be closely related.

4.1. The high temperature plasma (HP)

The most representative feature for the HP is the Fe XXV Kα line. Revnivtsev et al. (2009) resolved about 90% of the Fe Kα line at $(l, b) = (0^{\circ}\!.1, -1^{\circ}\!.4)$ into many point sources. This position is outside of the GCXE and rather in the GRXE (see figure 4 in Uchiyama et al. 2011). We therefore start the discussion with the assumption that the origin of the HP in the GRXE (not GCXE) may be the superposition of point sources. Uchiyama et al. (2011) compared the Fe XXV Kα line distribution with the stellar mass distribution (SMD) and found that the GCXE shows 3.8–19 times excess over the SMD that is normalized to the GRXE region. Since our observational results are essentially the same (but more extended), we will follow the discussion in Uchiyama et al. (2011).

The most probable candidate sources for the Fe XXV Kα line are cataclysmic variables (CVs) and active binaries (ABs) (e.g. Yuasa et al. 2012), because their spectra are represented by a high-temperature plasma with large equivalent widths of the 6.7 keV (Fe XXV Kα; hereafter, $EW_{6.7}$) and 6.97 keV lines (Fe XXVI Lyα; $EW_{6.9}$), asso-

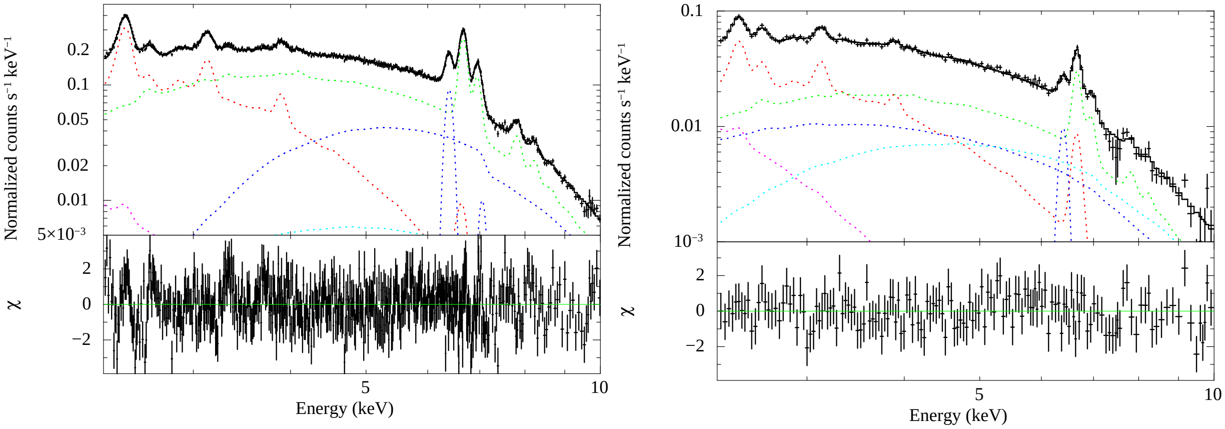

Fig. 8. NXB-subtracted X-ray spectra of the GCXE (left) and GRXE (right). The solid lines are the best-fit physical model (equation 5) for GCXE and GRXE. The dotted lines show APEC1 (green), APEC2 (red), CM (blue), CXB (cyan) and foreground (magenta) model components, respectively.

ciated with the 6.4 keV (Fe I Kα; $EW_{6.4}$) line, which are similar to those of the GRXE. The mean $EW_{6.4}$, $EW_{6.7}$ and $EW_{6.9}$ of the X-ray bright CVs in the luminosity range of 10^{30-33} erg s^{-1} are ∼100 eV, ∼200 eV and ∼100 eV, respectively (Ezuka & Ishida 1999, Rana et al. 2006). We further analyzed the Suzaku archive of ABs and found that their mean $EW_{6.4}$, $EW_{6.7}$ and $EW_{6.9}$ are ∼ 60 eV, ∼560 eV and ∼80 eV, respectively. On the other hand, our result (figure 8) shows that the mean $EW_{6.4}$, $EW_{6.7}$ and $EW_{6.9}$ in the GRXE are ∼110 eV, ∼490 eV and ∼110 eV, respectively. Thus, any mixture of the bright X-ray CVs and ABs cannot explain $EW_{6.7}$, $EW_{6.4}$ and $EW_{6.9}$ of the GRXE simultaneously. In order to explain by unresolved point sources, we need faint sources with lager equivalent widths of iron than those of the well-known CVs and ABs.

Unlike the GRXE, the majority of the GCXE has not been resolved into the point sources (Muno et al. 2004, Revnivtsev et al. 2007). Furthermore, the line intensity ratio of Fe XXVI Lyα/Fe XXV Kα is significantly larger in the GCXE than in the GRXE (see figure 6). Abundances are also different, 1.25 and 0.81 of the solar for the GCXE and GRXE, respectively. Therefore the GCXE is difficult to be explained by the same kind of point sources in the GRXE. We need different type of point sources with higher temperatures and abundances. This may be too artificial, and hence point source origin for the HP in the GCXE may not be favored.

One possibility is that a significant fraction of the HP would come from diffuse optically thin thermal plasma as already proposed by Koyama et al. (2007c) although small fraction of the HP in the GCXE is due to the same point source origin as that in the GRXE. The HP in the GCXE has the scale height of ∼40 pc ($0^\circ\!.27$) and the temperature of kT ∼7 keV (sound velocity ∼ 1500 km s^{-1}), and hence the dynamical age is $\sim 2\times10^4$ yr. The luminosity of the GCXE (5–8 keV) is 6×10^{35} erg s^{-1}, and the electron density is estimated to be ∼0.05 cc^{-1}. Hence the thermal energy of the HP is 1×10^{53} erg. If the diffuse plasma is made by multiple supernova (SN) explosions, the rate of SNe is estimated to be higher than 5×10^{-3} yr^{-1}. Since the mass in the GCXE HP region (∼40 pc × 90 pc) is ∼1% of the total mass of the Galaxy (e.g. Mezger et al. 1996, Launhardt et al. 2002), the SNe rate of 5×10^{-3} yr^{-1} is unreasonably high (see Diehl et al. 2006 and their supplement). Furthermore, the temperatures of supernova remnants (SNRs) of the age of $\sim 10^4$ yr is significantly lower than that of the HP (7 keV) in the GCXE, and hence the multiple-SN scenario would be unlikely.

Other possibility is that the HP in the GCXE may be made by violent flares of Sgr A* as suggested by Koyama et al. (1996). To produce such a high temperature (∼7 keV) and large scale (∼40 pc × 90 pc) plasma, many big flares would be necessary within the past 10^4 yr. The most recent big flare may be that in some 100 years ago at Sgr A*, which is well established by time variability of the 6.4 keV line from molecular clouds (Muno et al. 2007, Koyama et al. 2008, Inui et al. 2009, Koyama et al. 2009, Ponti et al. 2010, Nobukawa et al. 2011, Capelli et al. 2011, Capelli et al. 2012). Looking back to the older ages, the recent discovery of the "Fermi Bubble" (Su et al. 2010) may be responsible to some fraction of the HP.

4.2. The low temperature plasma (LP)

The low temperature plasma (LP) in the GRXE has been already reported by Kaneda et al. (1997). Our results are based on more extended and high quality data. The spatial distribution (scale length) of the LP is almost the same as the HP, but the scale height is larger than the HP. Kaneda et al. (1997) also reported a larger scale height of LP than that of HP, however their analysis did not separate the foreground emission of $kT = 0.6$ keV from the LP (see figure 7) , thus their scale height of the LP may be a subject of significant errors. Similar but slightly different LP is also found from the GCXE with the scale height is significantly larger than that of the HP

Using the best-fit distribution and plasma parameters, we estimated that the luminosity (2.3–5 keV), density and total energy of the LP in the GCXE are 5×10^{35} erg s^{-1}, 0.07 cc^{-1} and 1×10^{52} erg, respectively. In the GRXE, they are 6×10^{37} erg s^{-1}, 2×10^{-3} cc^{-1} and 5×10^{55} erg, respectively. From the LP temperature of $kT\sim1$ keV (sound velocity ~600 km s^{-1}) and the scale heights of ~55 pc ($b_{\mathrm{C}}\sim0.^{\circ}4$) and 550 pc ($b_{\mathrm{R}}\sim4^{\circ}$), the dynamical ages are estimated to be 9×10^{4} yr and 9×10^{5} yr, for the GCXE and GRXE, respectively.

The temperature of $kT\sim1$ keV is typically found in young and intermediate aged SNRs, and hence it may be conceivable that the plasma is due to multiple SNe within the past 10^{5} yr. To explain the total energy of the LP, the SN rate of 10^{-4} yr^{-1} and 0.5 yr^{-1} for the GCXE and GRXE would be required, respectively. For the GCXE, this number is not unreasonable. For the GRXE, the multiple-SN scenario alone is difficult to explain its origin. However, unlike the Fe Kα line, Revnivtsev et al. (2009) resolved less than 50% of the low energy band of the GRXE to point sources (see figure 2 in their paper), and hence the point source fraction in the LP in the GRXE would be smaller than those in the HP. Still some fraction of the LP in the GRXE would be due to point sources. Most probable candidate would be dwarf M stars (dMs), because these exhibit coronal activities with ~1 keV plasma and the number density is very high (Masui et al. 2009).

4.3. Fe I Kα emissions

This paper mainly targets highly ionized lines but we also comment about Fe I Kα line emissions a little. Clumpy and bright Fe I Kα line emissions in the Galactic center region have been studied well since the ASCA satellite (e.g. Koyama et al. 1996). Their origin is thought to be X-ray reflection nebulae (XRNe) irradiated by the past X-ray flare of Sgr A* due to their large EWs ($EW_{6.4}\sim1$ keV) and time variability (e.g. Koyama et al. 2007b, Inui et al. 2009). In this paper, we excluded these previously reported XRN regions from the GCXE spectra, and the EW to the associated continuum ($EW_{6.4}\sim460$ eV) is smaller than that of the XRN. The origin of the faint Fe I Kα emission in the GCXE might be different from that of the XRNe.

The origin of the Fe I Kα line in the GRXE is also not clear. One may argue that superpositions of CVs is one possibility, because CVs emit not only the Fe XXV Kα but also Fe I Kα lines. However, both the Fe XXV and Fe I Kα lines are hardly to be the same origin, because the scale height of the Fe I Kα line in the GRXE region is significantly smaller than that of the Fe XXV Kα line (see table 2).

The relatively smaller EW of $EW_{6.4}\sim460$ eV than that of XRNe may prefer the scenario that the origin is due to the interaction between high-energy electrons and interstellar neutral matter (e.g. Yusef-Zadeh et al. 2012). More quantitative details are beyond the scope of this paper.

5. Summery

We summarize the results of this paper as;

1. We have analyzed all the Suzaku archive in the Galactic plane within $|b|<5^{\circ}$.
2. We presented a global structure of the Galactic plane in the K-shell line intensities from highly ionized S, Ar, Ca and Fe as well as neutral Fe I and the continuum band in 2.3–5 and 5–8 keV.
3. We clearly separated the Galactic center X-ray emission (GCXE) from the Galactic ridge X-ray emission (GRXE) with the scale length (in the longitude) of $\sim0.^{\circ}6$ and $\sim50^{\circ}$, and the scale heights (in the latitude) of $\sim0.^{\circ}2$–$0.^{\circ}4$ and $\sim1^{\circ}$–5°, respectively.
4. The K-shell line intensity ratios of H-like and He-like ions (Lyα/Kα) suggest that the GCXE and GRXE plasmas have multi-temperature structures.
5. The Lyα/Kα profiles along the Galactic plane are different from element to element.
6. The most striking contrast of the Lyα profiles is found in the S and Fe atoms. The former shows almost no excess while the latter exhibits pronounced excess in the GCXE.
7. The spectra of the GCXE and GRXE are decomposed into two temperature plasmas of about 1 and 7 keV. The temperature of the 1-keV plasma in the GCXE is lower than that in GRXE, and vice versa for the 7-keV plasma.

The authors thank all of the Suzaku team members, especially T. Yuasa, and K. Makishima for their comments and useful information. We also thank V. Dogiel for improving the paper. HU is supported by Japan Society for the Promotion of Science (JSPS) Research Fellowship for Young Scientists. KK is supported by JSPS KAKENHI Grand Numbers 23000004 and 24540229. MN is supported by JSPS KAKENHI Grand for the young scientist (B), Number 24740123. This work was supported by the Grant-in-Aid for the Global COE Program “The Next Generation of Physics, Spun from Universality and Emergence” from the Ministry of Education, Culture, Sports, Science and Technology (MEXT) of Japan. This work was also supported by Grant-in-Aid of the JSPS Nos. 10243007 and 23340047.

References

Anders, E., & Grevesse, N. 1989, Geochim. Cosmochim. Acta, 53, 197

Capelli, R., Warwick, R. S., Porquet, D., Gillessen, S., & Predehl, P. 2011, A&A, 530, A38

Capelli, R., Warwick, R. S., Porquet, D., Gillessen, S., & Predehl, P. 2012, arXiv:1207.1436

Diehl, R., Halloin, H., Kretschmer, K., et al. 2006, Nature, 439, 4

Ebisawa, K., Maeda, Y., Kaneda, H., & Yamauchi, S. 2001, Science, 293, 1633

Ebisawa, K., et al. 2005, ApJ, 635, 214

Ebisawa, K., et al. 2008, PASJ, 60, 223

Ezuka, H. & Ishida, M. 1999, ApJS, 120, 277

Inui, T., Koyama, K., Matsumoto, H., & Tsuru, T. G. 2009, PASJ, 61, 241

Ishisaki, Y., et al. 2007, PASJ, 59, 113

Kaastra, J. S., & Mewe, R. 1993, A&AS, 97, 443
Kaneda, H., et al. 1997, ApJ, 491, 638
Koyama, K., Ikeuchi, S., & Tomisaka, K. 1986a, PASJ, 38, 503
Koyama, K., Makishima, K., Tanaka, Y., & Tsunemi, H. 1986b, PASJ, 38, 121
Koyama, K., Awaki, H., Kunieda, H., Takano, S., & Tawara, Y. 1989, Nature, 339, 603
Koyama, K., Maeda, Y., Sonobe, T., Takeshima, T., Tanaka, Y., & Yamauchi, S. 1996, PASJ, 48, 249
Koyama, K., et al. 2007a, PASJ, 59, 23
Koyama, K., et al. 2007b, PASJ, 59, 221
Koyama, K., et al. 2007c, PASJ, 59, 245
Koyama, K., Inui, T., Matsumoto, H., & Tsuru, T. G. 2008, PASJ, 60, 201
Koyama, K., Takikawa, Y., Hyodo, Y., Inui, T., Nobukawa, M., Matsumoto, H., & Tsuru, G. T. 2009, PASJ, 61, 255
Kushino, A., Ishisaki, Y., Morita, U., Yamasaki, N. Y., Ishida, M., Ohashi, T., & Ueda, Y. 2002, PASJ, 54, 327
Launhardt, R., Zylka, R., & Mezger, P. G. 2002, A&A, 384, 112
Masui, K., et al. 2009, PASJ, 61, 115
Mezger, P. G., Duschl, W. J., & Zylka, R. 1996, A&A Rev., 7, 289
Mitsuda, K., et al. 2007, PASJ, 59, 1
Morrison, R. & McCammon, D. 1983, ApJ, 270, 119
Muno, M. P., Baganoff, F. K., Bautz, M. W., et al. 2004, ApJ, 613, 326
Muno, M. P., Baganoff, F. K., Brandt, W. N., Park, S., & Morris, M. R. 2007, ApJL, 656, L69
Nakajima, H., et al. 2008, PASJ, 60, 1
Nobukawa, M., Koyama, K., Tsuru, T. G., Ryu, S. G., & Tatischeff, V. 2010, PASJ, 62, 423
Nobukawa, M., Ryu, S. G., Tsuru, T. G., & Koyama, K. 2011, ApJL, 739, L52
Ozawa, M., et al. 2009, PASJ, 61, 1
Ponti, G., Terrier, R., Goldwurm, A., Belanger, G., & Trap, G. 2010, ApJ, 714, 732
Prigozhin, G., Burke, B., Bautz, M., Kissel, S., & Lamarr, B. 2008, IEEE Transactions on Electron Devices, 55, 2111
Rana, V. R., Singh, K. P., Schlegel, E. M., & Barrett, P. E. 2006, ApJ, 642, 1042
Reid, M. J., & Brunthaler, A. 2004, ApJ, 616, 872
Revnivtsev, M., Molkov, S., & Sazonov, S. 2006, MNRAS, 373, L11
Revnivtsev, M., Vikhlinin, A., & Sazonov, S. 2007, A&A, 473, 857
Revnivtsev, M., Sazonov, S., Churazov, E., Forman, W., Vikhlinin, A., & Sunyaev, R. 2009, Nature, 458, 1142
Ryu, S. G., Koyama, K., Nobukawa, M., Fukuoka, R., & Tsuru, T. G. 2009, PASJ, 61, 751
Serlemitsos, P. J., et al. 2007, PASJ, 59, 9
Smith, R. K., Brickhouse, N. S., Liedahl, D. A., & Raymond, J. C. 2001, ApJL, 556, L91
Su, M., Slatyer, T. R., & Finkbeiner, D. P. 2010, ApJ, 724, 1044
Tawa, N., et al. 2008, PASJ, 60, 11
Uchiyama, H., et al. 2009, PASJ, 61, 9
Uchiyama, H., Nobukawa, M., Tsuru, T., Koyama, K., & Matsumoto, H. 2011, PASJ, 63, 903
Worrall, D. M., Marshall, F. E., Boldt, E. A., & Swank, J. H. 1982, ApJ, 255, 111
Warwick, R. S., Turner, M. J. L., Watson, M. G., & Willingale, R. 1985, Nature, 317, 218
Yamauchi, S., Kawada, M., Koyama, K., Kunieda, H., & Tawara, Y. 1990, ApJ, 365, 532
Yamauchi, S., & Koyama, K. 1993, ApJ, 404, 620
Yamauchi, S., Ebisawa, K., Tanaka, Y., Koyama, K., Matsumoto, H., Yamasaki, N. Y., Takahashi, H., & Ezoe, Y. 2009, PASJ, 61, 225
Yuasa, T., Makishima, K., & Nakazawa, K. 2012, ApJ, 753, 129
Yusef-Zadeh, F., et al. 2012, arXiv:1206.6882